PCCP

ROYAL SOCIETY OF CHEMISTRY

PAPER

View Article Online
View Journal | View Issue

Check for updates

Cite this: *Phys. Chem. Chem. Phys.*, 2026, **28**, 2294

Structure-function correlations in graphene screen-printed electrodes: capacitive and faradaic behaviour

Tharinda Kasemphong,[a] Monchai Jitvisate,[b] Chanida Jakkrawhad,[a] Wichayaporn Kamsong,[c] Chanpen Karuwan,[c] Pachanuporn Sunon,[d] Supinya Nijpanich,[e] Phanawan Whangdee,[f] Theeranun Siritanon[a] and Kamonwad Ngamchuea*[a]

How the origin of graphene influences interfacial behaviour once it is formulate and screen-printed has been unclear. Herein, we fabricate four graphene screen-printed electrodes (commercial, combustion-derived, exfoliated, and CVD-grown) using an identical ink and printing protocol and combine conventional electroanalysis with step-potential electrochemical spectroscopy to obtain assumption-light differential capacitance $C(E)$ and charging timescales τ. All electrodes show U-shaped $C(E)$ with tightly clustered PZCs (0.35–0.40 V *vs.* Ag/AgCl), indicating that the charge-neutral potential is set primarily by surface chemistry and electronic structure, rather than morphology. However, the extent and speed of interfacial charging vary. The double-layer capacitance (C_{dl}) scales with wetting and mesoporosity, while the charging time (τ = 15–25 ms across the set) reflects the trade-off between ionic access resistance and capacitance. For the partially inner-sphere redox couple $[Fe(CN)_6]^{4-/3-}$, heterogeneous electron transfer follows edge, defect, and oxygen functionality, rather than film conductivity, with k^0 spanning (0.76–1.99) $\times$ 10^{-5} m s^{-1}. These interfacial electrochemical metrics, both capacitive and faradaic, map directly onto physical features such as porosity, defect density, and interfacial chemistry, providing initial criteria for selecting graphene precursors in sensing, catalysis, and energy storage.

Received 4th October 2025,
Accepted 23rd December 2025

DOI: 10.1039/d5cp03833b

rsc.li/pccp

Published on 24 dicembre 2025. Downloaded on 03/05/2026 23:17:09.

1 Introduction

Screen-printed electrodes (SPEs) have emerged as indispensable components in electrochemical sensing and energy technologies, owing to their low production cost, high throughput, and suitability for miniaturized, disposable, and flexible platforms.[1,2] Among carbon-based materials, graphene has garnered considerable attention for SPE fabrication due to its excellent electrical conductivity, large specific surface area, and tunable surface chemistry.[3] Despite these advantages, a fundamental and unresolved question persists regarding the extent to which the method of graphene synthesis dictates its electrochemical performance when integrated into printed devices.

Graphene can be synthesized by a wide range of approaches, from bottom-up chemical vapour deposition (CVD) to top-down exfoliation and even low-cost combustion-derived routes.[4] Each method yields materials with distinct structural, chemical, and morphological features *e.g.* layer number, defect density, oxygen functionality, and stacking order that are known to influence double-layer charging and heterogeneous electron transfer (HET).[5] Notably, several studies report that single- and few-layer graphene do not necessarily outperform graphite in electroanalytical measurements as the higher edge density and interlayer defects in multilayer/graphite systems provide abundant active sites, stronger analyte adsorption, and lower noise/ohmic artifacts.[6]

Beyond layer count, porosity alters the apparent kinetics by creating thin-layer or confinement conditions. Overlapping diffusional fields in pores increase local residence time and near-surface concentration, which can sharpen peaks, reduce

[a] *School of Chemistry, Institute of Science, Suranaree University of Technology, 111 University Avenue, Suranaree, Muang, Nakhon Ratchasima 30000, Thailand. E-mail: kamonwad@g.sut.ac.th; Tel: +66 (0) 44 224 637*
[b] *School of Physics, Institute of Science, Suranaree University of Technology, 111 University Avenue, Suranaree, Muang, Nakhon Ratchasima 30000, Thailand*
[c] *National Nanotechnology Center (NANOTEC), National Science and Technology Development Agency (NSTDA), Pathum Thani 12120, Thailand*
[d] *Institute of Research and Development, Suranaree University of Technology, 111 University Avenue, Suranaree, Muang, Nakhon Ratchasima, 30000, Thailand*
[e] *Synchrotron Light Research Institute, 111 University Avenue, Suranaree, Muang, Nakhon Ratchasima, 30000, Thailand*
[f] *Department of Applied Physics, Faculty of Sciences and Liberal Arts, Rajamangala University of Technology Isan, Nakhon Ratchasima, 30000, Thailand*

This journal is © the Owner Societies 2026

Published on 24 dicembre 2025. Downloaded on 03/05/2026 23:17:09.

peak-to-peak separation (ΔE_p), and lower overpotentials, even when the intrinsic electron-transfer barrier is unchanged.[7] Defects such as vacancies, Stone–Wales motifs, and sp^2/sp^3 discontinuities introduce localized electronic states that enhance electronic coupling and adsorption for partially inner-sphere probes. However, excessive oxidation or disorder can increase charge-transfer resistance and promote site blocking.[8–10] Surface functionalization tunes work function, wettability, potential of zero charge (PZC), and specific adsorption; for example, oxygenated groups improve hydrophilicity and ion access but can form passivating surface complexes (*e.g.* with $[Fe(CN)_6]^{3-/4-}$), thereby slowing HET.[11,12] The edge-to-basal-plane ratio further governs density of states at the Fermi level and chemisorption propensity, with edge-rich carbons generally exhibiting faster HET than basal-plane-dominated materials.[13,14]

However, existing reports on graphene SPEs remain fragmented, often focusing on a single graphene source or emphasizing only either capacitive behaviour for supercapacitors or faradaic responses for redox probes, without systematically linking the two regimes. As a result, there is no unified understanding of how the intrinsic properties of graphene, dictated by its synthesis method, affect both the baseline capacitive properties and the electron transfer kinetics when integrated into practical SPE platforms. Furthermore, the dynamic evolution of electrode surface wetting under electrolyte exposure, which directly affects electrochemical responses, is rarely considered in the context of printed graphene electrodes. This knowledge gap carries important implications for both fundamental understanding and practical deployment.

Herein, we present a systematic assessment of the electrochemical behaviour of SPEs fabricated from four distinct graphene sources, combustion-derived, electrochemically exfoliated, CVD-grown, and commercial graphene, using an identical ink formulation and printing process. These sources reflect the range of graphene materials commonly used in printed electrochemical devices, including (bio)sensors, where ink formulation and graphene type affect sensitivity and reproducibility,[3,15] and energy devices such as flexible conductors and micro-/planar supercapacitors, where accessible surface area and interfacial resistance govern capacitance and rate performance.[16–19] Prior studies have further highlighted that graphene source can introduce significant variability, through factors such as binder interactions and residual metal impurities, which impact electron-transfer kinetics and capacitive behaviour in SPEs.[20]

By combining structural/chemical characterization with electrochemical analyses and contact-angle measurements in water and concentrated electrolytes over repeated use, our study links microscopic material features and wettability evolution to macroscopic electrode descriptors relevant to practical printed devices (*e.g.* ion access, double-layer charging, and redox kinetics), providing guidance for selecting graphene sources for sensing and energy-related SPE applications.

2 Experimental

2.1 Chemical reagents

All chemical reagents were used as received without further purification: potassium chloride (KCl, ≥99.0%, Sigma-Aldrich), potassium hexacyanoferrate(II) trihydrate ($K_4[Fe(CN)_6]\cdot 3H_2O$, ≥98.5%, Sigma-Aldrich), potassium hexacyanoferrate(III) ($K_3[Fe(CN)_6]$, ≥99.0%, Sigma-Aldrich), silver/silver chloride ink (C61003P7, Sun Chemical), carbon paste ink (C2030519P4, Sun Chemical), insulator ink (D2070423P5, Sun Chemical). Deionized water (18.2 MΩ cm) was obtained from an Elga Purelab Ultra system (Elga Labwater, UK). All experiments were conducted at 25 °C unless stated otherwise.

2.2 Graphene sources and synthesis

Four distinct types of graphene were investigated: commercial, combustion-derived, electrolytically exfoliated, and CVD-grown. Commercial graphene powder was purchased from UC Bacon Co. Ltd and used as received. Combustion-derived graphene was synthesized following an adaptation of Chen *et al.*[21] Briefly, 3.00 g of magnesium ribbon was placed on a slab of solid CO_2 (dry ice), ignited, and immediately covered with a second slab. Combustion in CO_2 produced MgO and a carbonaceous by-product. The black solid was collected and stirred in 100.0 mL of 1.00 M HCl at room temperature overnight to remove Mg/MgO, then filtered and rinsed with deionized water to neutral pH. The purified carbon was dried under high vacuum at 100 °C overnight to yield the combustion-derived graphene.[21]

Exfoliated graphene powder was prepared by one-step electrolytic exfoliation.[22] Two graphite rods served as electrodes in aqueous polystyrene sulfonate (PSS). A constant 8.0 V bias was applied for 24 h to exfoliate graphite into graphene sheets. The dispersion was washed with ethanol and deionized water to remove excess PSS/ions, then dried at 80 °C for 2 h.[22]

CVD graphene was grown on FeNi catalyst in a thermal CVD reactor. The FeNi catalyst was prepared by impregnation and reduced at 500 °C for 1 h under 1500 sccm H_2 to convert the oxide to its metallic form. The catalyst and a triglyceride-based lipid feedstock (used as the carbon source) were then loaded into a quartz tube furnace and heated to 800 °C at 10 °C min^{-1} under 1500 sccm N_2 flow. Growth proceeded for 1 h at 800 °C, after which the system was cooled to room temperature under 1500 sccm N_2. The resulting graphene was collected as powder for ink formulation (see below).

2.3 Fabrication of graphene screen-printed electrodes (SPEs)

A conductive graphene ink was prepared by blending 2.50 g of each type of graphene powder (commercial, combustion, exfoliated, or CVD) with 10.0 g of carbon paste ink in a ball mill (Retsch model Emax, Germany) at 1000 rpm for 60 min. Graphene screen-printed electrodes (SPEs) were fabricated on polyethylene terephthalate (PET) substrates using a screen printer (DEK model 03ix, USA). First, Ag/AgCl ink was screen-printed and dried at 60 °C for 5 min to form the reference electrode (RE). The formulated graphene ink was then printed and dried at 60 °C for 5 min to produce the working (WE) and

Published on 24 dicembre 2025. Downloaded on 03/05/2026 23:17:09.

counter (CE) electrodes. Finally, an insulator ink was printed to define the active electrode area and dried at 120 °C for 5 min. For each batch, a total of 600 SPEs were printed. The corresponding graphene loading is 4.17 mg per SPE.

2.4 Characterization

Surface morphology was imaged by field-emission scanning electron microscopy (FE-SEM, AURIGA, Zeiss; 3.0 kV). Crystallinity and stacking order were assessed by powder X-ray diffraction (XRD, D8 ADVANCE, Bruker; Cu K_α, λ = 1.5406 Å). Graphitic and defect signatures (D, G, 2D) were evaluated by Raman spectroscopy (VERTEX 70 with RAM II, Bruker). Surface composition was determined by X-ray photoelectron spectroscopy (XPS, PHI 5000 VersaProbe II, ULVAC-PHI; Al K_α, $h\nu$ = 1486.6 eV) at the SUT-NANOTEC-SLRI Joint Research Facility (SLRI, Thailand); spectra were processed in PHI MultiPak with Shirley backgrounds and mixed Gaussian–Lorentzian line shapes, using the C 1s peak at 284.8 eV for charge referencing. Textural properties were obtained from nitrogen adsorption–desorption at 77 K (Autosorb 6100, Anton Paar). The specific surface area was calculated by Brunauer–Emmett–Teller (BET) analysis. The pore volume was obtained by non-local density functional theory (NLDFT) physisorption analysis, a statistical-mechanics adsorption model in which the experimental isotherm is represented as a linear combination of theoretical adsorption isotherms computed for pores of different widths.[23–25] The mesopore size distribution was evaluated using the Barrett–Joyner–Halenda (BJH) analysis (desorption branch). Samples were degassed at 250 °C for 5 h before measurement.

2.5 Electrochemical measurements

Electrochemical studies were performed with an Autolab PGSTAT302N potentiostat (Metrohm, Netherlands). All potentials are reported *vs.* the on-chip Ag/AgCl unless stated otherwise. Electrochemical impedance spectroscopy (EIS) was performed in a 5.0 mM solution of $[Fe(CN)_6]^{3-/4-}$ containing 0.10 M KCl. Measurements were conducted across a frequency range of 1–10^5 Hz with an applied AC amplitude of 5 mV. Nyquist spectra were fitted to a Randles equivalent circuit to extract the charge-transfer resistance R_{ct}.

Time-resolved analysis of double-layer charging employed step-potential electrochemical spectroscopy (SPECS). Prior to measurements, electrodes were conditioned by 50 cyclic voltammetry (CV) cycles in 1.0 M KCl within a non-faradaic window.[26] A staircase of ±10 mV potential steps was then applied, and the resulting current–time transients were recorded for all steps and used to determine the double-layer capacitance (C_{dl}) and the differential capacitance $C(E)$ over the window range. The potential of zero charge (PZC) was identified as the potential at which $C(E)$ reached its minimum value.

Faradaic behaviour was evaluated by CV in a 1.0 mM $[Fe(CN)_6]^{4-}$ solution with 0.10 M KCl as the supporting electrolyte at scan rates of 10–200 mV s^{-1}. Peak current–scan-rate (Randles–Ševčík) analysis provided the electroactive area. The kinetic parameters were obtained from Nicholson analysis of ΔE_p for k^0 and mass-transport-corrected Tafel slopes for β, as detailed in the Results and discussion section.

3 Results and discussion

The graphene synthesis route imprints a distinct combination of structural order, defect density, surface chemistry and mesoscale connectivity, and these features jointly govern the electrochemical behaviour of SPEs. To resolve these links, we examined four representative materials, commercial, combustion-derived, exfoliated graphene, and CVD-grown graphene formulated and printed under identical conditions. By integrating materials characterization and electrochemical analysis, we map how layer stacking, defect/edge architecture and oxygen functionality affect electrolyte wetting and accessibility, the magnitude and potential-dependence of interfacial capacitance, and heterogeneous electron-transfer rates.

3.1 Structure, defects, and surface chemistry

3.1.1 Morphology. Commercial graphene (Fig. 1a) presents thin plate-like sheets with moderate wrinkling and relatively uniform restacking, consistent with partially reassembled graphitic domains. Combustion-derived graphene (Fig. 1b) shows a highly porous surface, typical of high-temperature carbonization.[27] Exfoliated graphene (Fig. 1c) forms stacked sheets with frequent folds and exposed edges. CVD graphene (Fig. 1d) exhibits planar basal-plane-dominated domains with low edge density and regions of loosely stacked fragments.

3.1.2 Crystallographic analysis. XRD patterns (Fig. 2a) resolve differences in out-of-plane stacking and in-plane order across the samples. In graphitic carbons, the (002) reflection reports interlayer spacing and stacking of the basal planes, whereas the (100) reflection arises from the hexagonal in-plane lattice of sp^2 carbon and is sensitive to in-plane coherence.[28] Commercial graphene shows a peak at 26.4° (002) and a small peak 43.7° (100), consistent with multilayer stacking. The combustion-derived sample exhibits features at 26.0° (002) and 42.8° (100); the relatively stronger (100) peak compared with the commercial sample suggests moderate in-plane order. Exfoliated graphene shows only the 26.6° (002) peak, consistent with stacked multilayers and limited in-plane coherence. CVD graphene shows a 26.3° (002) peak together with a modest 44.4° (100) feature, indicative of moderate in-plane ordering. Broadening and shifts of the (002) peak (*e.g.* 26.0° for combustion-derived *vs.* 26.6° for exfoliated) reflects slight variations in interlayer spacing (d_{002}), which can arise from oxygen functional groups or stacking disorder.

3.1.3 Raman spectroscopic analysis. Raman spectra (Fig. 2b) of all graphene SPEs exhibit the characteristic D, G and 2D bands, where the G band arises from the in-plane vibrational stretching of sp^2 carbon, the D band is a defect-activated ring-breathing mode, and the 2D band is the second-order (double-resonant) overtone of the D band which can indicate layer number. The commercial graphene gives ν_D = 1278.7 cm^{-1} and ν_G = 1602.7 cm^{-1}. The combustion-derived

 This journal is © the Owner Societies 2026

Published on 24 dicembre 2025. Downloaded on 03/05/2026 23:17:09.

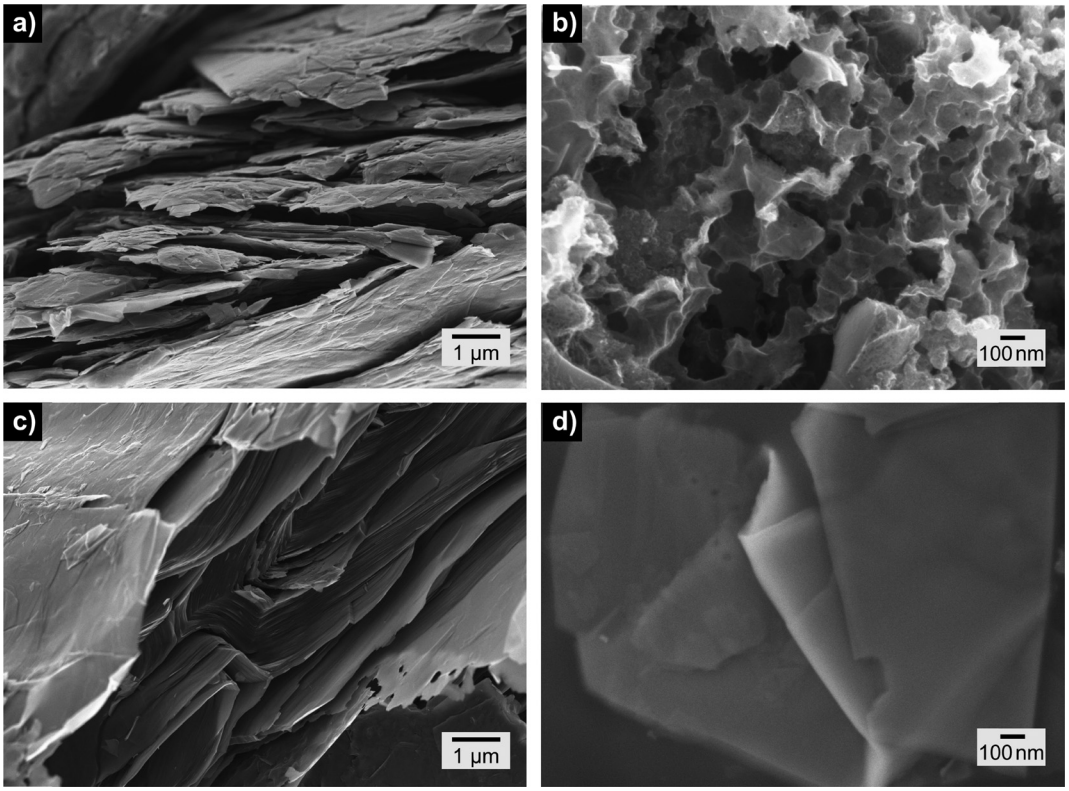

Fig. 1 SEM images of graphene from different synthesis routes: (a) commercial, (b) combustion-derived, (c) exfoliated, and (d) CVD-grown graphene.

sample is modestly upshifted in D and slightly downshifted in G with ν_D = 1284.5 cm^{-1} and ν_G = 1600.8 cm^{-1}. The exfoliated sample shows the largest D upshift with a G downshift with ν_D = 1296.1 cm^{-1} and ν_G = 1595.0 cm^{-1}. CVD graphene exhibits ν_D = 1290.3 cm^{-1}, ν_G = 1593.1 cm^{-1}. These trends are consistent with variations in strain and stacking order across the series, where a higher ν_G corresponds to fewer layers, and a lower ν_G is associated with multilayer graphene. The 2D band is sharper and more symmetric for the combustion and CVD samples, consistent with few-layer domains, whereas the commercial and exfoliated samples exhibit broader, less intense 2D bands consistent with multilayer stacking, supporting the interpretation from G-band shifts. The D/G intensity ratio (I_D/I_G) follows the trend: commercial (1.33) > combustion (1.18) ≈ CVD (1.16) > exfoliated (1.08), suggesting the highest defect density in the commercial sample and the lowest in the exfoliated sample, despite its multilayer structure.

3.1.4 Surface chemical composition. XPS (Fig. 2c) emphasizes route-dependent surface chemistry. Commercial graphene shows moderate sp^2 (75.36%) and oxygen (15.81% C–O, 3.03% C═O, 0.15% O–C═O).[29] Combustion-derived graphene retains high sp^2 (80.95%) with notable oxygen (10.98% C–O, 2.80% C = O, 5.27% O–C═O) and a distinctive O 1s feature (~531.0 eV) consistent with quinone-like groups.[30] Exfoliated graphene shows lower sp^2 (73.23%) with substantial oxygen functionalities (17.96% C–O, 3.07% C═O, 5.74% O–C═O), consistent with partial oxidation. CVD graphene exhibits the highest sp^2 carbon fraction (85.38%) and minimal oxygen (12.70% C–O, 1.92% C═O, 0% O–C═O).[31] These data therefore indicate how synthesis governs functional group distribution, which are the key determinants of interfacial and electrochemical behaviour.

3.2 Surface area and porosity characteristics

The surface area and porosity of the graphene SPEs were characterized by nitrogen adsorption–desorption at 77 K. Specific surface areas were determined using the Brunauer–Emmett–Teller (BET) method, total pore volumes from density functional theory (DFT) analysis, and mesopore size distributions from the Barrett–Joyner–Halenda (BJH) method. The resulting parameters are summarized in Table 1.

The combustion-derived graphene exhibits a Type IV isotherm, two orders of magnitude larger A_{BET}, and an order-of-magnitude larger V_{total} than the other samples, consistent with a mesoporous network created by disrupted stacking and interflake voids during high-temperature formation. In contrast, the commercial, exfoliated, and CVD materials show Type II isotherms with low A_{BET} and small V_{total}, indicative of largely nonporous or macroporous solids with limited accessible mesoporosity.

Across all samples, BJH returns similar mesopore radii (Table 1). For the combustion material, this reflects a dense population of small mesopores distributed throughout the network (hence high A_{BET} and V_{total}). For the Type II samples, the comparable r_{pore} should be interpreted as sparse slit-like gaps between restacked flakes. Although the radius is similar,

Published on 24 dicembre 2025. Downloaded on 03/05/2026 23:17:09.

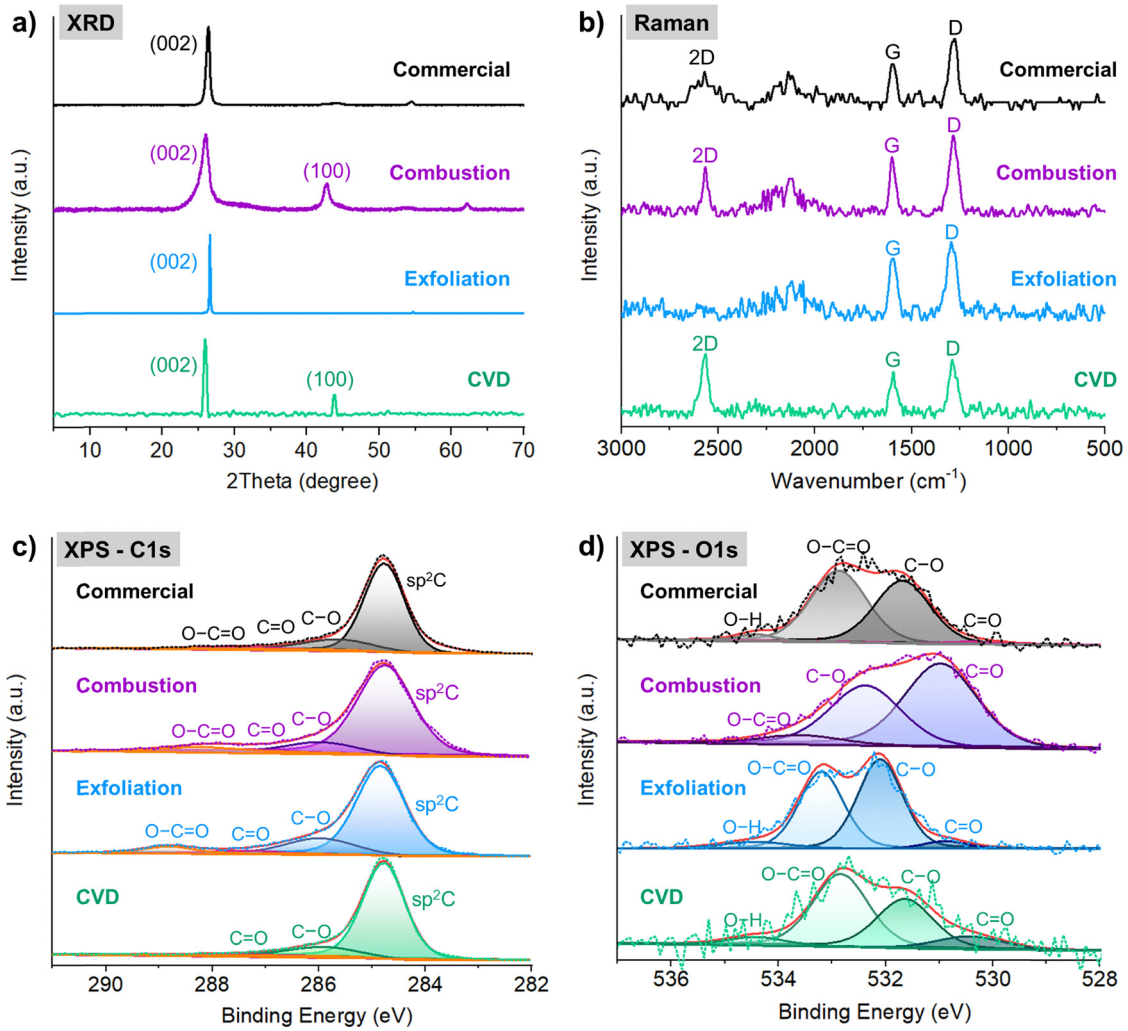

Fig. 2 (a) XRD patterns, (b) Raman spectra, (c) C 1s and (d) O 1s XPS spectra of commercial, combustion-derived, exfoliated, and CVD graphene.

the density of such features and therefore the accessible surface is much lower, as captured by A_{BET} and V_{total}.

However, only a fraction of A_{BET} contributes to the electrochemically active area, as access is limited by electrolyte penetration, wetting state, and electronic percolation to the current-carrying network. In concentrated electrolytes (*e.g.* 1.0 M KCl), the electrical double layer is sub-nanometer in thickness, enabling efficient charge storage in mesopores. In contrast, micropores are often underutilized in aqueous media owing to desolvation barriers and steric constraints. Studies have reported a threshold potential at which partial desolvation enables ion adsorption in these pores, which increases the capacitance C_{dl}.[32,33] The potential-dependent capacitance is further discussed in Section 3.4.

Table 1 Specific surface area, pore volume, and pore size of different graphene samples

	Isotherm	A_{BET}[a] ($m^2\ g^{-1}$)	V_{total}[b] ($cm^3\ g^{-1}$)	r_{pore}[b] (nm)
Commercial	Type II	29.2 ± 0.4	0.088	3.725
Combustion	Type IV	383.6 ± 2.4	0.856	3.838
Exfoliation	Type II	5.8 ± 0.1	0.012	3.789
CVD	Type II	14.3 ± 0.2	0.036	3.773

[a] A_{BET} reported as mean ± standard deviation. [b] V_{total} and r_{pore} reported as modal values.

3.3 Wetting behaviour and contact-angle evolution

All graphene SPEs exhibited similarly large water contact angles (θ_{H_2O} = 118–121°, Fig. 3), essentially independent of graphene type, indicating that initial wettability is dominated by the binder-rich surface which limits water affinity. Exposure to an electrolyte alters this interfacial state rapidly. In 1.0 M KCl, the apparent contact angle (θ_{KCl}) decreases upon reuse for every material, with cumulative first-to-second-use changes of 38.5° for combustion-derived ((118.1 ± 1.0)° → (79.6 ± 3.4)°), 34.5° for exfoliated graphene ((118.8 ± 1.3)° → (84.3 ± 3.9)°), 34.1° for commercial ((119.4 ± 0.6)° → (85.3 ± 1.8)°), and 25.5° for CVD graphene ((118.5 ± 2.0)° → (93.0 ± 5.6)°), refer to Fig. 3. In contrast, θ_{H_2O} changes only marginally between the first and second use, highlighting that wettability is governed primarily by ion–surface interactions rather than water.

 This journal is © the Owner Societies 2026

Published on 24 dicembre 2025. Downloaded on 03/05/2026 23:17:09.

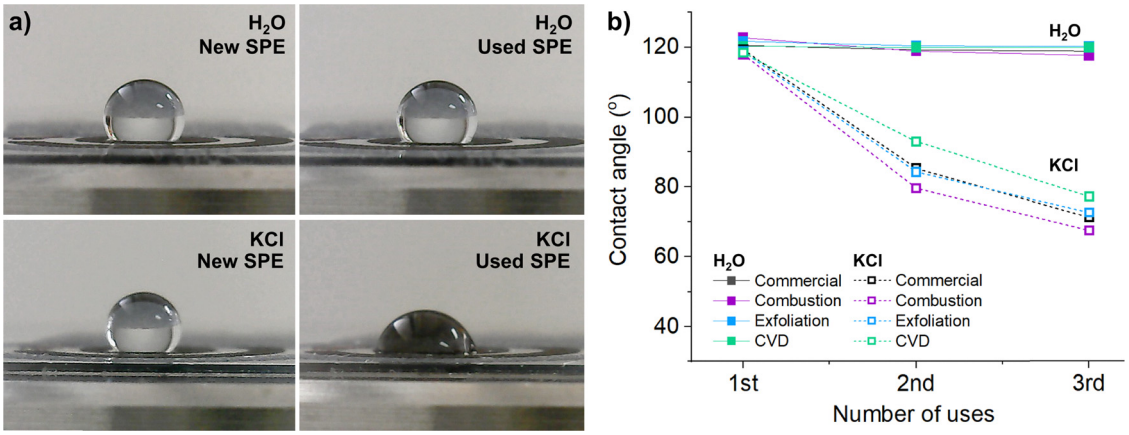

Fig. 3 (a) Representative images of DI water and 1.0 M KCl droplets on combustion-derived graphene SPEs. (b) Contact angle as a function of use number for all graphene SPEs measured with DI water and 1.0 M KCl.

The dependence of the macroscopic angle on interfacial tensions is given by Young's equation,

$$\gamma_{SV} - \gamma_{SL} = \gamma_{LV}\cos\theta_Y, \quad (1)$$

where γ_{SV}, γ_{SL}, and γ_{LV} are the solid–vapour, solid–liquid, and liquid–vapour interfacial tensions, and θ_Y is the intrinsic (Young) angle. Electrolyte exposure lowers γ_{SL} through specific ion adsorption and rearrangement of interfacial solvation, so that $\cos\theta_Y$ increases and the apparent angle decreases.[34] In 1 : 1 electrolytes such as KCl, the electrostatic screening (Debye) length is extremely short ($\kappa^{-1} \approx 0.3$ nm at 1.0 M KCl and 298 K), which promotes close approach of ions/water to polar/oxygenated sites and thus further reduces γ_{SL}. In addition, the intrinsic roughness and inter-flake voids of printed films favour capillary infiltration. As trapped air is replaced by liquid, the real solid–liquid contact fraction increases, and the macroscopic angle falls accordingly.[35,36]

The material-dependent ranking in changes in contact angle ($\Delta\theta_{KCl}$) is consistent with their structural and chemical attributes. The combustion-derived graphene combines abundant oxygenated sites with a dense, accessible mesopore population, enabling extensive electrolyte infiltration and therefore most effectively increases the true solid–liquid contact fraction. Exfoliated and commercial graphene, which are oxygen-rich and edge-dense, provides numerous polar sites (C–O, C═O, O–C═O) that lower the solid–liquid interfacial free energy *via* hydrogen bonding and specific adsorption of hydrated ions (particularly K^+ at negatively polarized/oxygenated sites), therefore also producing a large drop in θ_{KCl}. In contrast, CVD graphene, dominated by cleaner basal planes with minimal oxygen functionality and fewer capillary pathways, offers fewer sites for ion–surface interactions and exhibits the smallest wetting response, and hence the most angle-stable.

To isolate ion-identity effects beyond graphene type, we further measured contact angles for additional 1 : 1 electrolytes using the combustion-derived graphene SPE. The first use yields similarly high contact angles across all salts (θ = 119–121°), reinforcing that the initial state is binder-dominated. Upon reuse, however, the wetting evolution becomes strongly ion-specific. In the cation series at fixed Cl^- (LiCl, NaCl, KCl, RbCl), the cumulative decrease over repeated use is modest for Li^+ ($\Delta\theta$ = 24.5°) and Na^+ ($\Delta\theta$ = 25.0°), but becomes larger for K^+ ($\Delta\theta$ = 38.5°) and Rb^+ ($\Delta\theta$ = 47.8°), consistent with enhanced specific-ion contributions for larger, more weakly hydrated and more polarizable cations that can more effectively lower the effective γ_{SL} and promote greater penetration into interflake voids during repeated wetting. In the anion series at fixed K^+ (KCl, KBr, KI), the corresponding decreases follow Cl^- ($\Delta\theta$ = 38.5°) > Br^- ($\Delta\theta$ = 24.5°) > I^- ($\Delta\theta$ = 5.9°), indicating that anion identity also strongly controls how readily the interface transitions to a more wetted state upon reuse. Notably, prior studies on hydrophobic interfaces emphasise that specific-ion trends can be system- and mechanism-dependent and may not follow a single universal ordering, reflecting a combination of ion-specific interfacial affinity and dynamic interfacial processes. Practically, these data show that while the initial contact angle is set by the printed binder layer, the evolution of wetting with reuse is governed by ion-specific interactions and interfacial partitioning previously reported for hydrophobic/aqueous interfaces.[37–39]

3.4 Electrical transport

Four-point probe measurements establish a clear conductivity hierarchy for the printed graphene films: combustion (6.50 ± 1.21 kS m^{-1}) > CVD (4.46 ± 1.65 kS m^{-1}) > commercial (3.42 ± 1.34 kS m^{-1}) > exfoliated (2.72 ± 1.18 kS m^{-1}). These values are in the same order of magnitude with other reported graphene/carbon inks.[16,40–43] The high conductivity of the combustion graphene suggests an efficient percolation network with strong interflake coupling, likely aided by broad flake sizes and partial graphitization that maximize lateral contacts and minimize resistive junctions. CVD graphene, although intrinsically highly conductive, shows lower conductivity possibly due to folds and grain boundaries interrupt long-range pathways. The mesoscale assembly and interflake contact quality therefore dominate macroscopic transport in printed films,[36] outweighing the intrinsic properties of the graphene source.

Published on 24 dicembre 2025. Downloaded on 03/05/2026 23:17:09.

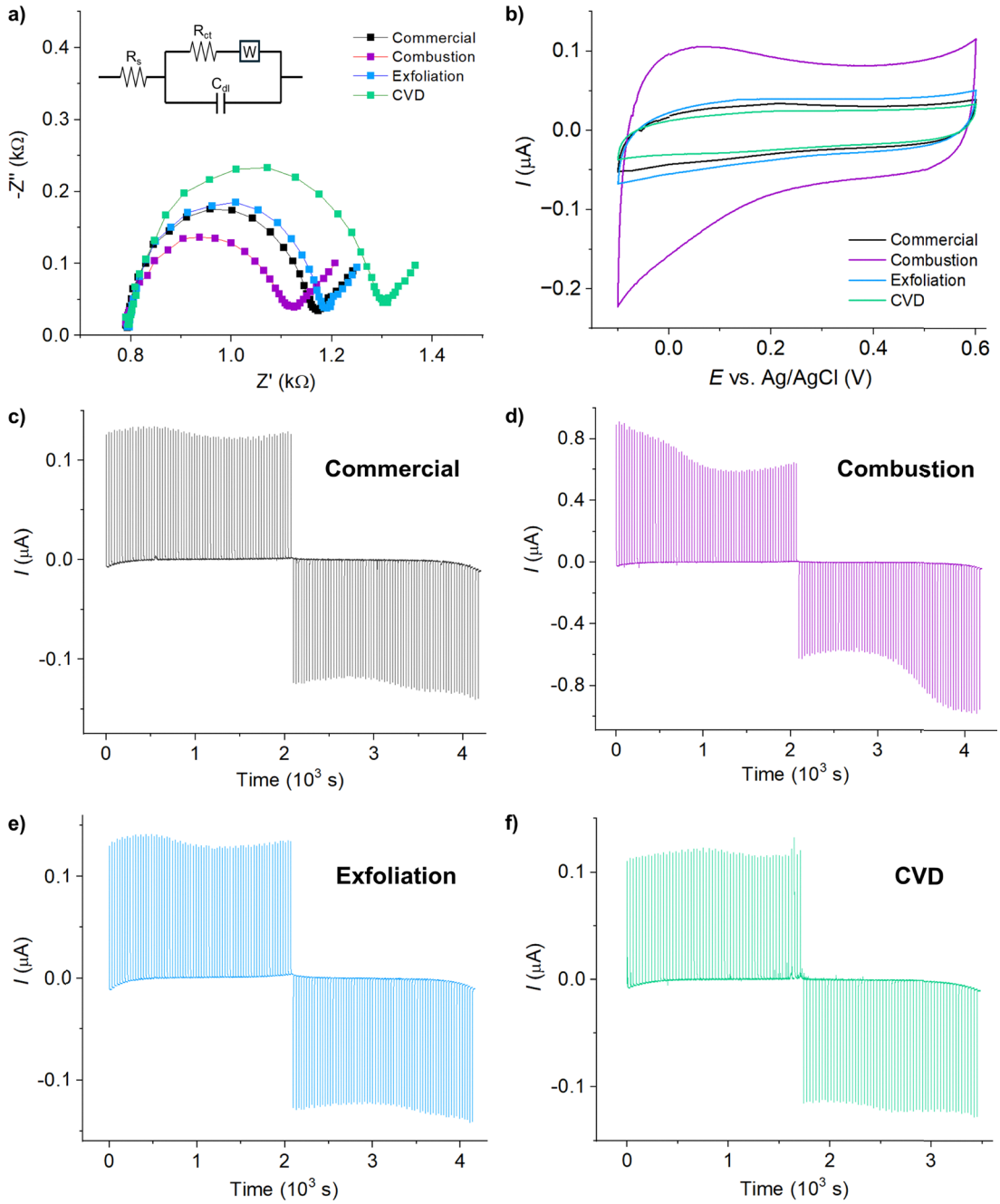

Fig. 4 (a) EIS spectra in 5.0 mM $[Fe(CN)_6]^{3-/4-}$ in 0.10 M KCl; frequency range 1 to 10^5 Hz, AC amplitude 5 mV for all graphene SPEs. (b) CV in blank 1.0 M KCl for all graphene SPEs; scan rate 25 mV s^{-1}. SPECS dataset in 1.0 M KCl showing a staircase of ±10 mV potential steps and the corresponding *I*–*t* transients of (c) commercial, (d) combustion-derived, (e) exfoliated, and (f) CVD-grown graphene.

Commercial and exfoliated graphene deliver moderate conductivities, consistent with smaller lateral domains, limited π-conjugation, higher edge fraction, and oxygenated groups that raise tunneling barriers.

3.5 Charge transfer resistance

Electrochemical impedance spectroscopy (EIS) of graphene SPEs was recorded in 5.0 mM $[Fe(CN)6]^{3-/4-}$ with 0.10 M KCl (AC amplitude 5 mV; 1–10^5 Hz). Nyquist plots (Fig. 4a) show a small high-frequency intercept (solution resistance, R_s), a semicircle at intermediate frequencies associated with interfacial charge transfer, and a low-frequency diffusional tail. Spectra were fitted with a Randles-type equivalent circuit (Fig. 4a, inset). The extracted charge-transfer resistances (R_{ct}) are 295 ± 14 Ω for combustion, 354 ± 6 Ω for commercial, 368 ± 36 Ω for exfoliated, and 474 ± 13 Ω for CVD graphene.

Two points follow directly from these data. First, there is no direct correlation between R_{ct} and the bulk film conductivity (Section 3.4). For example, the CVD electrode exhibits relatively high electrical conductivity yet the largest R_{ct}, indicating that

 This journal is © the Owner Societies 2026

Published on 24 dicembre 2025. Downloaded on 03/05/2026 23:17:09.

through-film transport does not dictate interfacial charge-transfer rates. Second, the R_{ct} ranking mirrors trends in wetting behaviour and porosity (Section 3.3), with the combustion-derived sample showing the lowest R_{ct} due to a combination of high mesoporosity, good electrolyte accessibility, and a surface enriched in edge and defect sites. In contrast, the CVD sample, composed largely of smooth basal planes with low oxygen functionality and minimal capillary infiltration, displays the highest R_{ct}.

These observations therefore indicate that charge-transfer performance in printed graphene electrodes is governed by interfacial site chemistry and electrolyte accessibility rather than bulk conductivity. Related parameters such as double-layer capacitance (Section 3.6) and kinetic constants (Section 3.7) further quantify these interfacial effects.

3.6 Capacitive behaviour

The electrochemical double-layer (EDL) behaviour of the graphene SPEs was evaluated by CV in 1.0 M KCl across a non-faradaic window. After 50 consecutive scans to stabilize the interfacial structure, the voltammograms retained an ideal rectangular shape (Fig. 4b), confirming that double-layer charging dominates under these conditions. These CV data provide an overview of the interfacial capacitance and motivate a transient analysis to resolve how charge is stored in space and time.

To deconvolute the interfacial processes, we employed step potential electrochemical spectroscopy (SPECS), where a staircase of small potential steps (±10 mV) yields current–time transients, each fitted to ref. 26

$$I_T = I_{dl} + I_d + I_r, \tag{2}$$

where I_T is the total current, I_{dl} is the capacitive (double-layer) current, I_d is the mass-transport current arising from ionic diffusion/migration in the electrolyte, and I_r is the residual/background current, covering small offsets for slow, quasi-steady processes not captured by the two terms above *e.g.* trace impurities, instrument leakage, *etc.*

The double-layer term captures capacitive charging immediately after each step, and is described by:

$$I_{dl} = \frac{\Delta E}{R_{dl}} \exp\left(-\frac{t}{\tau}\right), \tag{3}$$

$$\tau = R_{dl} C_{dl}, \tag{4}$$

where ΔE is the step amplitude, t is time, R_{dl} is the effective double-layer charging resistance, τ is the charging time constant, and C_{dl} is the interfacial double-layer capacitance. Although porous carbons can exhibit bi-exponential capacitive decays (outer-surface *vs.* pore-confined charging), introducing a second exponential here did not improve the fits and led to poorly identifiable parameters. In 1.0 M KCl the diffuse layer is ultrathin, so outer-surface charging is effectively single-time-constant at our time resolution; the slower relaxation is captured by the mass-transport term I_d, while I_r accounts for any residual offset.

The slower relaxation of the near-surface concentration field is captured by a semi-infinite diffusion term:

$$I_d = a_1 \left(1 + 2\sum_{k=1}^{\infty} \exp\left(-k^2 a_2 t\right)\right), \tag{5}$$

$$a_1 = \frac{FD\Delta c}{h}, \tag{6}$$

$$a_2 = \frac{\pi^2 D}{h^2}, \tag{7}$$

where F is the Faraday constant, D the diffusion coefficient, Δc the interfacial concentration gradient, and h the effective diffusion layer thickness ($k = 1$).

A direct comparison of the I–t transients in Fig. 4(c)–(f) provides insight into how each printed graphene electrode stores and releases charge under identical perturbations. The initial current immediately after each step reflects the magnitude of interfacial charging (*i.e.* electrolyte-accessible capacitance/area), while the decay rate reflects the longer-range charging/ion-access and hence how rapidly the interface stabilizes, which is relevant to rate performance in energy storage and response times in sensing. Any persistent offsets or drift indicate non-ideal background contributions that can compromise baseline stability in low-signal sensing. These qualitative differences motivate the quantitative fitting described below to extract C_{dl}, R_{dl}, and τ (and their potential dependence) for comparison across graphene sources.

Analyzing the measured charging current with eqn (2) results in fitting parameters that are used for surface charge calculation in the following procedure. The surface charge of the jth potential step can be determined by

$$\sigma_j = \int_0^{t'} (I_{dl} + I_d)\mathrm{d}t, \tag{8}$$

where t' is the step duration (30 s).

The cumulative summation of the surface charge at each potential step yields the potential-dependent surface charge:

$$\sigma(E) = \sum_j \sigma_j, \tag{9}$$

Differentiating the charge *vs.* potential directly gives the differential capacitance defined as

$$C(E) = \left(\frac{\partial \sigma}{\partial E}\right)_{T,\mu}, \tag{10}$$

where E is the electrode potential, T is temperature, and μ is the chemical potential.[44] This method provides an assumption-free differential capacitance unlike EIS or CV, where the obtained capacitance values strongly depend on the designed equivalent circuit models and appropriate assumptions.

The differential capacitance curves $C(E)$ are shown in Fig. 5. These capacitance values are reported as measured from SPECS transients and are not normalized by surface area; both BET-derived area and electroactive surface area metrics are provided in Table 2 for reference. The overall appearance of the curves in most cases is U-like shape, which can be expected

Published on 24 dicembre 2025. Downloaded on 03/05/2026 23:17:09.

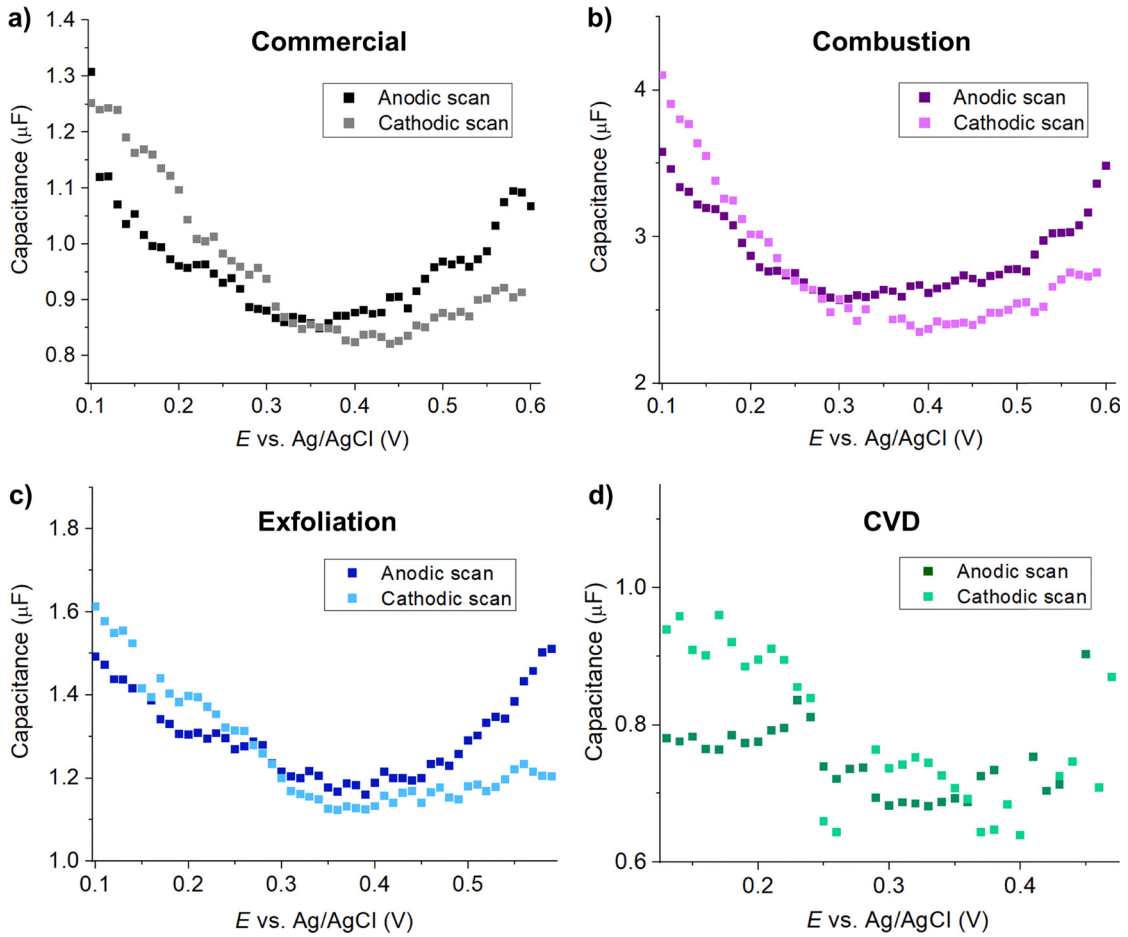

Fig. 5 Interfacial double-layer capacitance as a function of potential extracted from SPECS in 1.0 M KCl for (a) commercial, (b) combustion-derived, (c) exfoliated, and (d) CVD-grown graphene.

from carbon/aqueous electrolyte systems. Note that we scanned the electrode potential in both cathodic and anodic directions to observe whether the hysteresis occurs in our studied systems. It is clear from the plots that our $C(E)$ data exhibits, if not identical, similar trend for both scan directions in all cases, indicating very small hysteresis. It must also be noted here that the measured capacitance is the total capacitance of the series combination of the electrolyte double layer capacitance and the electrode capacitance. Since carbon, unlike perfect metal, is known to have limited density of states. This gives rise to the

Table 2 Summary of physicochemical and interfacial electrochemical properties of different graphene SPEs

					Surface functionality				
Graphene type	Morphology	Edge exposure	Layers	Defect level	sp^2 C (%)	C–O (%)	C═O (%)	O–C═O (%)	A_{BET} ($m^2\ g^{-1}$)
(A) Structural and chemical properties									
Commercial	Stacked sheets	High	Multi-layer	High	75.36	15.81	3.03	0.15	29.2 ± 0.4
Combustion	Mesoporous	High	Few-layer	Moderate	80.95	10.98	2.80	5.27	383.6 ± 2.4
Exfoliation	Stacked sheets	High	Multi-layer	Low	73.23	17.96	3.07	5.74	5.8 ± 0.1
CVD	Sheet	Low, mostly basal	Few-layer	Moderate	85.38	12.70	1.92	0.00	14.3 ± 0.2

		θ_{KCl} (°)							
Graphene type	σ (kS m^{-1})	1st	2nd	PZC (V)	C_{dl} (μF)	R_{ct} (Ω)	$A_{CV,rev}$ (10^{-6} m^2)	k^0 (10^{-5} m s^{-1})	β
(B) Electronic, wetting, and interfacial electrochemical properties									
Commercial	3.42 ± 1.34	119.4 ± 0.6	85.3 ± 1.8	0.40 ± 0.06	0.83 ± 0.02	354 ± 6	8.02 ± 0.08	1.03 ± 0.06	0.86 ± 0.01
Combustion	6.50 ± 1.21	118.1 ± 1.0	79.6 ± 3.4	0.38 ± 0.01	2.47 ± 0.17	295 ± 14	8.71 ± 0.03	1.20 ± 0.09	0.83 ± 0.01
Exfoliation	2.72 ± 1.18	118.8 ± 1.3	84.3 ± 3.9	0.39 ± 0.01	1.14 ± 0.03	368 ± 36	8.43 ± 0.10	1.99 ± 0.26	0.81 ± 0.01
CVD	4.46 ± 1.65	118.5 ± 2.0	93.0 ± 5.6	0.35 ± 0.04	0.64 ± 0.02	474 ± 13	7.82 ± 0.04	0.76 ± 0.03	0.76 ± 0.01

Note: All SPE types have the same graphene mass loading per electrode (4.17 mg graphene per SPE).

 This journal is © the Owner Societies 2026

Published on 24 dicembre 2025. Downloaded on 03/05/2026 23:17:09.

penetration of an electric field into the materials, generating the space charge polarization. With this in mind, if one of the capacitances of the two components is considerably smaller than another one, it will be pronounced in the total capacitance.

From the $C(E)$ profile, the potential of zero charge (PZC) is located at the minimum of $C(E)$. PZCs cluster narrowly at 0.38–0.40 V *vs.* Ag/AgCl for all the graphene SPEs (commercial 0.40 ± 0.06 V, exfoliated 0.39 ± 0.01 V, combustion 0.38 ± 0.01 V, CVD 0.35 ± 0.04 V). The relatively invariant PZC reflects the fact that it is primarily dictated by the surface chemical composition, such as functional groups and specific ion adsorption.

Although the PZC varies modestly, the capacitance at the PZC differs markedly: commercial 0.83 ± 0.02 μF, combustion 2.47 ± 0.17 μF, exfoliated 1.14 ± 0.03 μF, and CVD 0.64 ± 0.02 μF. Normalized by the electroactive surface area (determined using $[Fe(CN)_6]^{4-/3-}$ in the next section), the average specific capacitances are 10.3, 32.3, 13.5, and 8.3 μF cm^{-2} for commercial, combustion, exfoliated, and CVD, respectively, typical of well-wetted carbons in aqueous electrolyte.[45] The commercial and exfoliated electrodes show comparable capacitance, consistent with their similar surface structures, whereas combustion graphene exhibits over two-fold increase in capacitance, indicating a distinct surface structure that enhances electrolyte accessibility, and this result may indicate the role of surface structure in modulating capacitive behaviour in carbon materials.[46]

In the high-ionic-strength limit (Debye length ≪ pore size), pores larger than a few nanometres host non-overlapping double layers. Under these conditions, C_{dl} scales with the electrolyte-accessible surface area rather than with the total surface area measured by gas adsorption (A_{BET}).[47] Improved wetting increases the contact area between electrolyte and electrode but does not alter the intrinsic surface potential at which net charge vanishes. Consequently, significant changes in C_{dl} can occur without appreciable shifts in PZC.

The charging resistances at the PZC further differentiate the electrodes: R_{dl} (PZC) = 6.1 ± 0.4 kΩ (combustion), 22.1 ± 0.6 kΩ (exfoliated), 28.6 ± 0.7 kΩ (commercial), and 30.5 ± 0.9 kΩ (CVD). Therefore, the combustion graphene couples high C_{dl} with low R_{dl}, indicative of a percolated, well-wetted pore network, whereas the CVD film combines the smallest C_{dl} with the largest R_{dl}, consistent with limited electrolyte accessibility and high access resistance.

The corresponding charging time constant (τ) lies in the 15–25 ms range across electrodes (Fig. 6), explaining why CVs

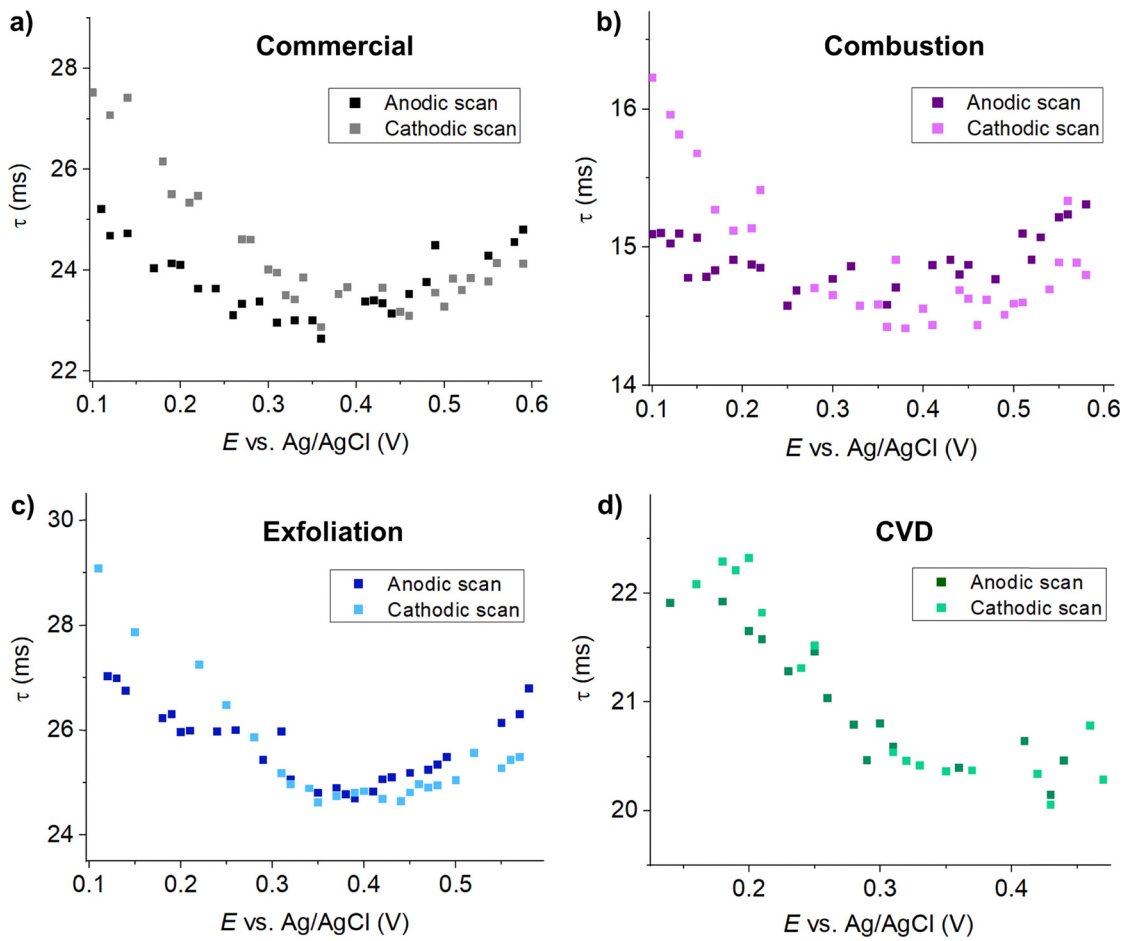

Fig. 6 Charging time constant (τ) as a function of potential extracted from SPECS in 1.0 M KCl for (a) commercial, (b) combustion-derived, (c) exfoliated, and (d) CVD-grown graphene.

Published on 24 dicembre 2025. Downloaded on 03/05/2026 23:17:09.

appear nearly rectangular at relatively slow scan rates ($t \gg \tau$). $\tau(E)$ exhibits shallow U-shaped profiles that mirror $C(E)$ with minima occur near the PZC. Considering $C(E)$ alongside $\tau(E)$ separates how much charge is stored from how fast it is stored. Combustion graphene exhibits high C_{dl} with the smallest R_{dl} and τ, consistent with rapid, well-accessed charging. Thus, porosity does not necessarily slow charging. While microporous or poorly wetted carbons can produce long, multi-exponential relaxations, a mesoporous, well-wetted architecture, as in this combustion material, can reduce R_{dl} enough to shorten τ even as C_{dl} increases. Commercial and exfoliated electrodes show intermediate τ, consistent with comparable surface structures and moderate R_{dl}. CVD graphene with the smallest C_{dl} but the largest R_{dl} shows comparatively slow charging due to limited accessibility.

3.7 Faradaic behaviour

The $[Fe(CN)_6]^{4-/3-}$ redox couple, while formally reversible, is well recognized to proceed *via* a partially inner-sphere electron transfer pathway on carbon-based electrodes, rendering its kinetics highly sensitive to surface chemistry and local microstructure.[11,13] This property makes it an ideal probe for elucidating interfacial differences among printed graphene electrodes. Representative cyclic voltammograms collected at 50 mV s^{-1} (Fig. 7a) revealed subtle but reproducible variations in peak shape and separation across the different types of graphene, suggesting differences in their ability to facilitate electron exchange. Further investigation of the scan rate dependence (10–200 mV s^{-1}), illustrated in Fig. 7b for the combustion-derived system, showed linear increases in peak current with the square root of the scan rate (Fig. 7b, inset), confirming a diffusion-controlled process for all electrode types.

The electroactive surface area (A) was initially estimated using the reversible Randles–Ševčík relationship (eqn (11)),[48] giving comparable values across the electrodes: (8.02 ± 0.08) × 10^{-6} m^2 for commercial, (8.71 ± 0.03) × 10^{-6} m^2 for combustion, (8.43 ± 0.10) × 10^{-6} m^2 for exfoliated, and (7.82 ± 0.04) × 10^{-6} m^2 for CVD graphene. Estimates using the totally irreversible limiting form (eqn (12), with $\beta = 0.5$) are larger in all cases: (1.44 ± 0.01) × 10^{-5} m^2 for commercial, (1.57 ± 0.01) × 10^{-5} m^2 for combustion, (1.52 ± 0.02) × 10^{-5} m^2 for exfoliated, and (1.41 ± 0.01) × 10^{-5} m^2 for CVD graphene. To evaluate these limiting assumptions, we performed numerical simulations (refer to SI) and found that the experimental response lies between the reversible and totally irreversible limits, consistent with quasi-reversible behaviour of $[Fe(CN)_6]^{4-/3-}$. Therefore,

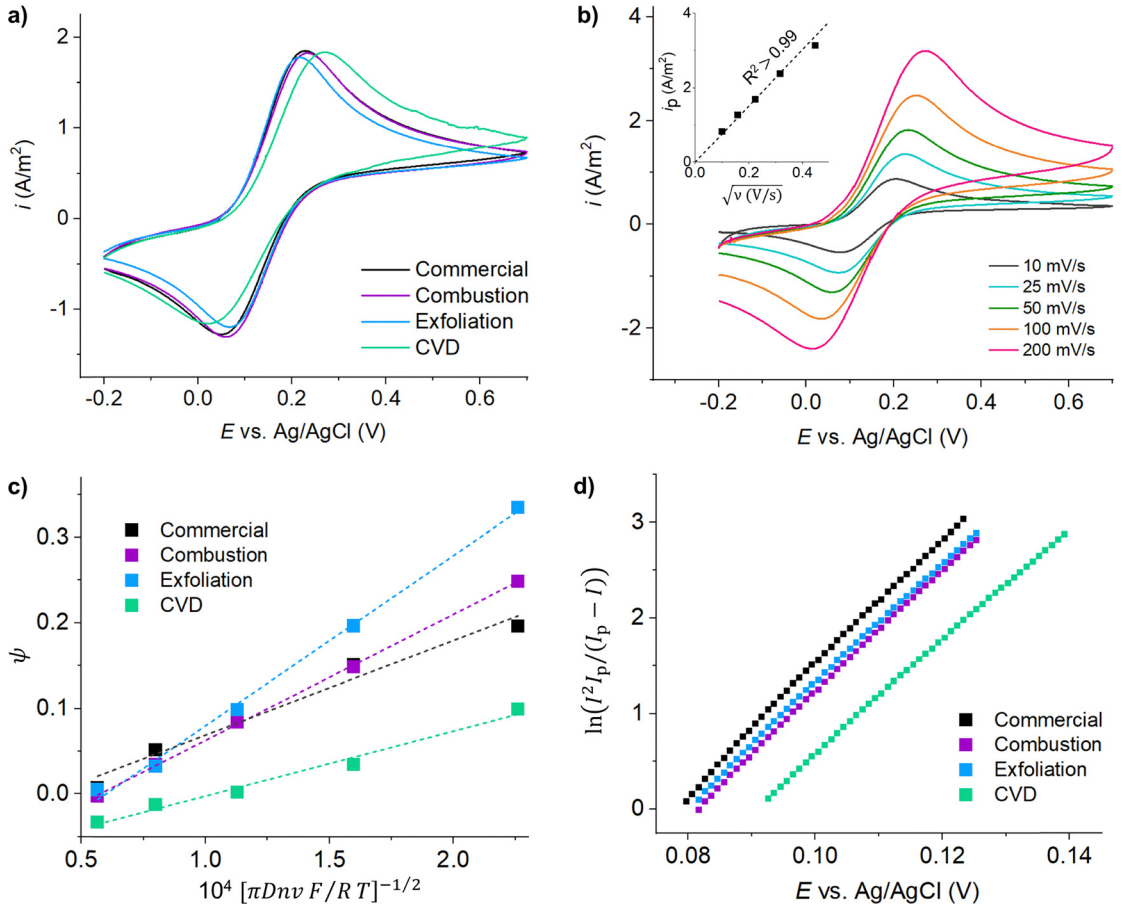

Fig. 7 (a) CV of 1.0 mM $[Fe(CN)_6]^{4-}$ in 0.10 M KCl recorded at a scan rate of 50 mV s^{-1} for all graphene SPEs. (b) Representative scan-rate studies for a combustion-derived graphene SPE. (inset: Randles–Ševčík linearity of i_p with $\sqrt{\nu}$). (c) Nicholson analysis and (d) mass-transport-corrected Tafel analysis for all graphene SPEs.

 This journal is © the Owner Societies 2026

Published on 24 dicembre 2025. Downloaded on 03/05/2026 23:17:09.

neither limiting form is appropriate for accurate determination of A. Nonetheless, applying a single expression consistently across all electrodes provides a useful comparative ('apparent') electroactive area for benchmarking between SPE types.

$$I_p = 0.446nFAc^* \sqrt{\frac{nFDv}{RT}}, \quad (11)$$

$$I_p = 0.496\sqrt{n' + \beta}nFAc^* \sqrt{\frac{F\nu D}{RT}}, \quad (12)$$

where I_p is the peak current, n is the total number of electron transfer, A is the electroactive surface area, c^* is the bulk concentration, v is the scan rate, F is the Faraday constant (96 485 C mol^{-1}), D is the diffusion coefficient, R is the universal gas constant (8.314 J K^{-1} mol^{-1}), T is the absolute temperature, n' is the number of electron transfer before the rate-determining step, and β is the anodic transfer coefficient of the rate-determining step.

To quantify kinetic differences, the apparent heterogeneous electron-transfer rate constant (k^0) was extracted using Nicholson's approach:[49,50]

$$\psi = (-0.6288 + 0.021\Delta E_p)/(1 - 0.017\Delta E_p), \quad (13)$$

where ΔE_p is the peak-to-peak separation, which is utilized to determine ψ in:

$$\psi = k^0[\pi DnvF/RT]^{-1/2}, \quad (14)$$

where ψ is a kinetic parameter, n is the number of electrons process, D is the diffusion coefficient ($D = 6.67 \times 10^{-10}$ m^2 s^{-1} for $[Fe(CN)_6]^{4-}$),[51] F is the Faraday constant (96 485 C mol^{-1}), υ is the potential scan rate, R is the universal gas constant (8.314 J K^{-1} mol^{-1}), and T is the temperature.

The exfoliated graphene electrode exhibited the highest rate constant, at $(1.99 \pm 0.26) \times 10^{-5}$ m s^{-1}, significantly outperforming the CVD-based electrode, which showed the lowest value of $(0.76 \pm 0.03) \times 10^{-5}$ m s^{-1}. The combustion-derived and commercial electrodes demonstrated intermediate behaviour, with k^0 values of $(1.20 \pm 0.09) \times 10^{-5}$ m s^{-1} and $(1.03 \pm 0.06) \times 10^{-5}$ m s^{-1}, respectively. These values fall within the established range for graphene-based electrodes and are consistent with prior reports demonstrating that electron transfer kinetics for $[Fe(CN)_6]^{4-/3-}$ vary significantly with graphene type and structure.[5,52–54] Notably, literature comparisons show k^0 values of 1.81×10^{-5}, 3.25×10^{-5}, 19.3×10^{-5}, and 53.2×10^{-5} m s^{-1} for monolayer graphene, quasi-graphene, basal-plane pyrolytic graphite (BPPG), and edge-plane pyrolytic graphite (EPPG), respectively.[13] This well-established trend confirms that k^0 scales with the abundance of edge sites and surface defects that facilitate inner-sphere pathways.

The superior performance of the exfoliated and combustion-derived graphene electrodes can be rationalized by their structural features: both materials comprise multilayer graphene[55] with a high density of exposed edge planes, defect sites, and surface functionalities; factors known to enhance electronic coupling and enable more facile redox interactions.[54] In contrast, CVD-grown graphene predominantly consists of few-layer structures with extensive basal-plane coverage and minimal edge exposure. This leads to significantly slower kinetics, as basal planes are intrinsically less reactive toward partially inner-sphere redox couples like $[Fe(CN)_6]^{4-/3-}$.

The underlying reason for the kinetic trends lies in how activation energy for electron transfer is modulated by the electrode's surface features. According to Butler–Volmer and transition state theory, the activation energy for the anodic process of $[Fe(CN)_6]^{4-/3-}$ (n = 1) under applied overpotential (η) is:

$$\Delta G^{\ddagger} = \Delta G_0^{\ddagger} - \beta F\eta, \quad (15)$$

where $\Delta G_0^{\ddagger}$ is the activation energy at equilibrium and β is the transfer coefficient, which reflects the symmetry of the energy barrier. A high k^0 indicates both a low intrinsic $\Delta G_0^{\ddagger}$ and favorable surface coupling. The exfoliated and combustion-derived electrodes, rich in edge and defect sites, are structurally primed to lower the activation barrier and facilitate electron exchange.

We also estimated β using mass-transport-corrected Tafel analysis:[56]

$$\frac{\partial \ln\left(\frac{I^2 I_p}{I_p - I}\right)}{\partial E} = \frac{2F(n' + \beta)}{RT}, \quad (16)$$

This analysis was performed on the rising edge of the first anodic wave (10–48% of the peak current (I_p)), a region where capacitive and diffusional contributions are minimal and the faradaic process dominates. E is the electrode potential, n' is the number of electron transfer before the rate-determining step (n' = 0 for the $[Fe(CN)_6]^{4-/3-}$ system), β is the anodic transfer coefficient of the rate-determining step, R is the molar gas constant (8.314 J K^{-1} mol^{-1}), F is the Faraday constant (96 485 C mol^{-1}), and T is the absolute temperature.

The apparent anodic transfer coefficients (β) derived from this treatment were 0.86 ± 0.01 for commercial, 0.83 ± 0.01 for combustion, 0.81 ± 0.01 for exfoliated, and 0.76 ± 0.01 for CVD graphene. However, the experimental voltammograms are highly symmetric and simulations that reproduce the peak positions and overall wave shape are best described by $\beta \approx 0.5$ for all electrodes (refer to SI). We therefore treat the Tafel-derived β values as apparent parameters, noting that surface heterogeneity, uncompensated resistance, and deviations from the ideal assumptions can bias the extracted slopes. In contrast, the observed variation in k^0 is robust and is attributed primarily to differences in electronic coupling and the density/distribution of electroactive sites, rather than changes in β.

Table 2 consolidates the structural, wetting, capacitive, and kinetic parameters for the four graphene SPEs, enabling direct comparison of trends discussed in Sections 3.3–3.7 and Fig. 3–7. This synopsis highlights the co-variation of interfacial electrochemical metrics with porosity, edge and defect density, and surface chemistry.

Published on 24 dicembre 2025. Downloaded on 03/05/2026 23:17:09.

4 Conclusions

Using a common ink formulation and printing protocol, we have shown that the graphene synthesis route dictates route-specific electrochemical behaviour in SPEs. All materials exhibit U-shaped $C(E)$ with narrowly clustered PZCs (0.35–0.40 V *vs.* Ag/AgCl), indicating that surface chemistry and electronic structure, rather than morphology, sets the charge-neutral potential. Nevertheless, the magnitude and kinetics of charging diverge: combustion-derived graphene combines the highest C_{dl} with the lowest, R_{dl}, yielding the fastest interfacial charging, whereas CVD shows the opposite, consistent with limited electrolyte accessibility. In sufficiently supported electrolyte (Debye length $\ll$ pore size), C_{dl} scales with electrolyte-accessible area rather than A_{BET}, and improved wetting increases C_{dl} without shifting PZC. For the partially inner-sphere couple $[Fe(CN)_6]^{4-/3-}$, heterogeneous electron transfer follows edge and defect abundance: exfoliated $\gtrsim$ combustion $>$ commercial $\gg$ CVD, while bulk film conductivity is a poor predictor of interfacial kinetics. Overall, $C(E)$ and $\tau(E)$ quantify charge storage and charging timescales, and k^0 captures kinetic facility, providing rigorous criteria to prioritize open, well-wetted mesoporosity for rapid charging and edge-rich, moderately functionalized surfaces for inner-sphere sensing, principles directly transferable to printed carbon electrodes for sensing, energy storage, and electrocatalysis.

Conflicts of interest

The authors declare no known competing financial interests or personal relationships that could have appeared to influence the work reported in this paper.

Data availability

The data used to support the findings of this study are included within the manuscript.

Supplementary information (SI) is available. See DOI: https://doi.org/10.1039/d5cp03833b.

Acknowledgements

This work is supported by (i) Suranaree University of Technology (SUT), (ii) Thailand Science Research and Innovation (TSRI) and (iii) National Science, Research and Innovation Fund (NSRF) (NRIIS number 215530).

References

1 J. P. Metters, R. O. Kadara and C. E. Banks, New directions in screen printed electroanalytical sensors: an overview of recent developments, *Analyst*, 2011, **136**(6), 1067–1076.
2 P. Fanjul-Bolado, D. Hernández-Santos, P. J. Lamas-Ardisana, A. Martín-Pernía and A. Costa-García, Electrochemical characterization of screen-printed and conventional carbon paste electrodes, *Electrochim. Acta*, 2008, **53**(10), 3635–3642.
3 E. P. Randviir, D. A. Brownson, J. P. Metters, R. O. Kadara and C. E. Banks, The fabrication, characterisation and electrochemical investigation of screen-printed graphene electrodes, *Phys. Chem. Chem. Phys.*, 2014, **16**(10), 4598–4611.
4 M. S. A. Bhuyan, M. N. Uddin, M. M. Islam, F. A. Bipasha and S. S. Hossain, Synthesis of graphene, *Int. Nano Lett.*, 2016, **6**(2), 65–83.
5 A. Ambrosi, C. K. Chua, A. Bonanni and M. Pumera, Electrochemistry of graphene and related materials, *Chem. Rev.*, 2014, **114**(14), 7150–7188.
6 M. S. Goh and M. Pumera, Single-, few-, and multilayer graphene not exhibiting significant advantages over graphite microparticles in electroanalysis, *Anal. Chem.*, 2010, **82**(19), 8367–8370.
7 C. Punckt, M. A. Pope, J. Liu, Y. Lin and I. A. Aksay, Electrochemical performance of graphene as effected by electrode porosity and graphene functionalization, *Electroanalysis*, 2010, **22**(23), 2834–2841.
8 P. Wei, J. Shen, K. Wu and N. Yang, Defect-dependent electrochemistry of exfoliated graphene layers, *Carbon*, 2019, **154**, 125–131.
9 Y. Jia, L. Zhang, A. Du, G. Gao, J. Chen, X. Yan, C. L. Brown and X. Yao, Defect graphene as a trifunctional catalyst for electrochemical reactions, *Adv. Mater.*, 2016, **28**(43), 9532–9538.
10 S. K. Tiwari, S. K. Pandey, R. Pandey, N. Wang, M. Bystrzejewski, Y. K. Mishra and Y. Zhu, Stone–Wales defect in graphene, *Small*, 2023, **19**(44), 2303340.
11 X. Ji, C. E. Banks, A. Crossley and R. G. Compton, Oxygenated edge plane sites slow the electron transfer of the ferro-/ferricyanide redox couple at graphite electrodes, *ChemPhysChem*, 2006, **7**(6), 1337–1344.
12 R. Jain and S. Mishra, Electrical and electrochemical properties of graphene modulated through surface functionalization, *RSC Adv.*, 2016, **6**(33), 27404–27415.
13 D. A. C. Brownson, S. A. Varey, F. Hussain, S. J. Haigh and C. E. Banks, Electrochemical properties of CVD grown pristine graphene: monolayer- vs. quasi-graphene, *Nanoscale*, 2014, **6**(3), 1607–1621.
14 C. C. Neumann, C. Batchelor-McAuley, C. Downing and R. G. Compton, Anthraquinone monosulfonate adsorbed on graphite shows two very different rates of electron transfer: surface heterogeneity due to basal and edge plane sites, *Chem. – Eur. J.*, 2011, **17**(26), 7320–7326.
15 S. Cinti and F. Arduini, Graphene-based screen-printed electrochemical (bio) sensors and their applications: Efforts and criticisms, *Biosens. Bioelectron.*, 2017, **89**, 107–122.
16 P. He, J. Cao, H. Ding, C. Liu, J. Neilson, Z. Li, I. A. Kinloch and B. Derby, Screen-Printing of a Highly Conductive Graphene Ink for Flexible Printed Electronics, *ACS Appl. Mater. Interfaces*, 2019, **11**(35), 32225–32234.
17 T. Sang Tran, N. K. Dutta and N. Roy Choudhury, Graphene-based inks for printing of planar micro-supercapacitors: a review, *Materials*, 2019, **12**(6), 978.

 This journal is © the Owner Societies 2026

Published on 24 dicembre 2025. Downloaded on 03/05/2026 23:17:09.

18 Y. Wang, X. Zhang, Y. Zhu, X. Li and Z. Shen, Planar micro-supercapacitors with high power density screen-printed by aqueous graphene conductive ink, *Materials*, 2024, **17**(16), 4021.
19 Y. Wang, X. Zhang, Y. Zhu, X. Li and Z. Shen, Planar Micro-Supercapacitors with High Power Density Screen-Printed by Aqueous Graphene Conductive Ink, *Materials*, 2024, **17**(16), 4021.
20 J. P. Smith, C. W. Foster, J. P. Metters, O. B. Sutcliffe and C. E. Banks, Metallic impurities in graphene screen-printed electrodes can influence their electrochemical properties, *Electroanalysis*, 2014, **26**(11), 2429–2433.
21 A. Chakrabarti, J. Lu, J. C. Skrabutenas, T. Xu, Z. Xiao, J. A. Maguire and N. S. Hosmane, Conversion of carbon dioxide to few-layer graphene, *J. Mater. Chem.*, 2011, **21**(26), 9491–9493.
22 C. Karuwan, A. Wisitsoraat, D. Phokharatkul, C. Sriprachuabwong, T. Lomas, D. Nacapricha and A. Tuantranont, A disposable screen printed graphene–carbon paste electrode and its application in electrochemical sensing, *RSC Adv.*, 2013, **3**(48), 25792–25799.
23 R. Bardestani, G. S. Patience and S. Kaliaguine, Experimental methods in chemical engineering: specific surface area and pore size distribution measurements—BET, BJH, and DFT, *Can. J. Chem. Eng.*, 2019, **97**(11), 2781–2791.
24 J. Landers, G. Y. Gor and A. V. Neimark, Density functional theory methods for characterization of porous materials, *Colloids Surf., A*, 2013, **437**, 3–32.
25 N. A. Seaton, J. P. R. B. Walton and N. quirke, A new analysis method for the determination of the pore size distribution of porous carbons from nitrogen adsorption measurements, *Carbon*, 1989, **27**(6), 853–861.
26 S. B. Davey, A. P. Cameron, K. G. Latham and S. W. Donne, Electrical double layer formation on glassy carbon in aqueous solution, *Electrochim. Acta*, 2021, **386**, 138416.
27 H. Nishihara, H. Fujimoto, H. Itoi, K. Nomura, H. Tanaka, M. T. Miyahara, P. A. Bonnaud, R. Miura, A. Suzuki and N. Miyamoto, Graphene-based ordered framework with a diverse range of carbon polygons formed in zeolite nanochannels, *Carbon*, 2018, **129**, 854–862.
28 C. Rao, K. Biswas, K. Subrahmanyam and A. Govindaraj, Graphene, the new nanocarbon, *J. Mater. Chem.*, 2009, **19**(17), 2457–2469.
29 T. Reiss, K. Hjelt and A. Ferrari, Graphene is on track to deliver on its promises, *Nat. Nanotechnol.*, 2019, **14**, 907–910.
30 S. J. R. Prabakar, Y.-H. Hwang, B. Lee, K.-S. Sohn and M. Pyo, Graphene-Sandwiched $LiNi_{0.5}Mn_{1.5}O_4$ Cathode Composites for Enhanced High Voltage Performance in Li Ion Batteries, *J. Electrochem. Soc.*, 2013, **160**(6), A832.
31 A. Shchukarev and D. Korolkov, XPS Study of group IA carbonates, *Open Chem.*, 2004, **2**(2), 347–362.
32 J. E. Zuliani, S. Tong, D. W. Kirk and C. Q. Jia, Isolating the effect of pore size distribution on electrochemical double-layer capacitance using activated fluid coke, *J. Power Sources*, 2015, **300**, 190–198.
33 G. Sun, W. Song, X. Liu, D. Long, W. Qiao and L. Ling, Capacitive matching of pore size and ion size in the negative and positive electrodes for supercapacitors, *Electrochim. Acta*, 2011, **56**(25), 9248–9256.
34 L. Zhao, Y. Li, M. Yu, Y. Peng and F. Ran, Electrolyte-wettability issues and challenges of electrode materials in electrochemical energy storage, energy conversion, and beyond, *Adv. Sci.*, 2023, **10**(17), 2300283.
35 M. Razavifar, A. Abdi, E. Nikooee, O. Aghili and M. Riazi, Quantifying the impact of surface roughness on contact angle dynamics under varying conditions, *Sci. Rep.*, 2025, **15**(1), 16611.
36 F. Torrisi, T. Hasan, W. Wu, Z. Sun, A. Lombardo, T. S. Kulmala, G.-W. Hsieh, S. Jung, F. Bonaccorso and P. J. Paul, Inkjet-printed graphene electronics, *ACS Nano*, 2012, **6**(4), 2992–3006.
37 V. Craig, B. Ninham and R. M. Pashley, Effect of electrolytes on bubble coalescence, *Nature*, 1993, **364**(6435), 317–319.
38 L. Meagher and V. S. Craig, Effect of dissolved gas and salt on the hydrophobic force between polypropylene surfaces, *Langmuir*, 1994, **10**(8), 2736–2742.
39 C. L. Henry and V. S. Craig, The link between ion specific bubble coalescence and Hofmeister effects is the partitioning of ions within the interface, *Langmuir*, 2010, **26**(9), 6478–6483.
40 Y. Lee, S. B. Park, K.-W. Kim, H. Jo, J. K. Kim, S. H. Kim, S. Lim, S. W. Lee and C.-H. Choi, Effective and Scalable Graphene Ink Production for Printed Microsupercapacitors, *Ind. Eng. Chem. Res.*, 2025, **64**(14), 7507–7515.
41 L. W. T. Ng, X. Zhu, G. Hu, N. Macadam, D. Um, T.-C. Wu, F. Le Moal, C. Jones and T. Hasan, Conformal Printing of Graphene for Single- and Multilayered Devices onto Arbitrarily Shaped 3D Surfaces, *Adv. Funct. Mater.*, 2019, **29**(36), 1807933.
42 D. Wang, W. Zhang, J. Wang, X. Li and Y. Liu, A high-performance, all-solid-state Na^+ selective sensor printed with eco-friendly conductive ink, *RSC Adv.*, 2023, **13**(24), 16610–16618.
43 M. Wang, J. Wang, A. Wei, X. Li, W. Zhang and Y. Liu, Highly stable aqueous carbon-based conductive ink for screen-printed planar flexible micro-supercapacitor, *J. Alloys Compd.*, 2024, **976**, 173125.
44 A. J. Bard, L. R. Faulkner and H. S. White, *Electrochemical methods: fundamentals and applications*, John Wiley & Sons, 2022.
45 H. Ji, X. Zhao, Z. Qiao, J. Jung, Y. Zhu, Y. Lu, L. L. Zhang, A. H. MacDonald and R. S. Ruoff, Capacitance of carbon-based electrical double-layer capacitors, *Nat. Commun.*, 2014, **5**(1), 3317.
46 J. Meyer, S. Hamwi, M. Kröger, W. Kowalsky, T. Riedl and A. Kahn, Transition metal oxides for organic electronics: energetics, device physics and applications, *Adv. Mater.*, 2012, **24**(40), 5408–5427.
47 G. Salitra, A. Soffer, L. Eliad, Y. Cohen and D. Aurbach, Carbon electrodes for double-layer capacitors I. Relations

Published on 24 dicembre 2025. Downloaded on 03/05/2026 23:17:09.

between ion and pore dimensions, *J. Electrochem. Soc.*, 2000, **147**(7), 2486.

48 R. G. Compton and C. E. Banks, *Understanding voltammetry*, World Scientific, 2018.

49 R. Agarwal, The Nicholson Method of Determination of the Standard Rate Constant of a Quasireversible Redox Couple Employing Cyclic Voltammetry: Everything One Needs to Know!, *ACS Electrochem.*, 2025, **1**(10), 1885–1894.

50 I. Lavagnini, R. Antiochia and F. Magno, An extended method for the practical evaluation of the standard rate constant from cyclic voltammetric data, *Electroanalysis*, 2004, **16**(6), 505–506.

51 S. Konopka and B. McDuffie, Diffusion coefficients of ferri- and ferrocyanide ions in aqueous media, using twin-electrode thin-layer electrochemistry, *Anal. Chem.*, 1970, **42**(14), 1741–1746.

52 D. H. Angell and T. Dickinson, The kinetics of the ferrous/ferric and ferro/ferricyanide reactions at platinum and gold electrodes: Part I. Kinetics at bare-metal surfaces, *J. Electroanal. Chem. Interfacial Electrochem.*, 1972, **35**(1), 55–72.

53 J. Hui, X. Zhou, R. Bhargava, A. Chinderle, J. Zhang and J. Rodríguez-López, Kinetic Modulation of Outer-Sphere Electron Transfer Reactions on Graphene Electrode with a Sub-surface Metal Substrate, *Electrochim. Acta*, 2016, **211**, 1016–1023.

54 M. Velický, D. F. Bradley, A. J. Cooper, E. W. Hill, I. A. Kinloch, A. Mishchenko, K. S. Novoselov, H. V. Patten, P. S. Toth, A. T. Valota, S. D. Worrall and R. A. W. Dryfe, Electron Transfer Kinetics on Mono- and Multilayer Graphene, *ACS Nano*, 2014, **8**(10), 10089–10100.

55 D. A. Brownson, L. J. Munro, D. K. Kampouris and C. E. Banks, Electrochemistry of graphene: not such a beneficial electrode material?, *RSC Adv.*, 2011, **1**(6), 978–988.

56 D. Li, C. Lin, C. Batchelor-McAuley, L. Chen and R. G. Compton, Tafel analysis in practice, *J. Electroanal. Chem.*, 2018, **826**, 117–124.

 This journal is © the Owner Societies 2026